

UKAEA-CCFE-PR(18)48

Viacheslav Kuksenko, Steve Roberts and Edmund Tarleton

Nanoindentation hardness anisotropy of beryllium

Enquiries about copyright and reproduction should in the first instance be addressed to the UKAEA Publications Officer, Culham Science Centre, Building K1/0/83 Abingdon, Oxfordshire, OX14 3DB, UK. The United Kingdom Atomic Energy Authority is the copyright holder.

Nanoindentation hardness anisotropy of beryllium

Viacheslav Kuksenko,^{1,2} Steve Roberts¹ and Edmund Tarleton¹

¹Department of Materials, University of Oxford, Parks Road, Oxford, UK, OX1 3PH

²UKAEA, Culham Science Centre, Abingdon, Oxon, OX14 3DB, UK

Nanoindentation hardness anisotropy of beryllium

Viacheslav Kuksenko^{1), 2)}, Steve Roberts¹⁾, Edmund Tarleton¹⁾

Department of Materials, University of Oxford, Parks Road, Oxford, UK, OX1 3PH

UKAEA, Culham Science Centre, Abingdon, Oxon, OX14 3DB, UK

* Corresponding author: slava.kuksenko@ukaea.uk

Abstract

Four industrial beryllium grades were tested via nanoindentation. An extremely high variation of hardness was observed in all samples. Analysis of the nanoindentation data in combination with SEM/EBSD measurements demonstrated that the crystallographic orientation of the indented grain was the major source of the wide variation in hardness, which was 2.5 times higher when the indentation direction was close to the [0001] c-axis of beryllium compared to indentation along the [11 $\bar{2}$ 0] or [1 $\bar{1}$ 00] directions. Crystal plasticity finite-element (CPFEM) simulations indicated how this hardness anisotropy arises from the anisotropy in the plastic deformation. Experiments and simulations also demonstrated that localised plastic deformation of the surface around the indent (pile-up or sink-in) was highly crystallographically dependent: during indentation into “soft” orientations, pile-up dominated; while sink-in behaviour was dominant during indentation into “hard” orientation. This implies that the hardness values calculated from indenter displacement and indenter profile using the standard Oliver-Pharr approach, without considering pile-up/sink-in effects, will be incorrect. Several contact area correction methods were applied and are compared. In contrast the indentation modulus was not found to have any strong crystallographic dependence. CPFEM analysis indicates that this is due to the complex 3-dimensional nature of the elastic interaction between the indenter and the sample, and also since, for the chosen indentation depth, the elastic interaction volume is much larger than the materials’ grain size.

Key words: beryllium, hardness, anisotropy, nanoindentation, crystal plasticity, CPFEM, pile-up, sink-in, contact area correction.

1 Introduction

Beryllium has a unique combination of mechanical and physical properties, including low density, low nuclear interaction cross-section, high strength and melting point combined with superior heat conductivity (D. Webster, 2012; Walsh, 2009). It is successfully used in a wide variety of applications involving severe environmental conditions, such as nuclear facilities, military aircraft and aerospace (*Design Guides for Materion Beryllium Metal*, 2017). .

Indentation is widely used for characterization of local mechanical properties of materials. It has been successfully used for beryllium for investigating the evolution of properties at different temperatures (Tsuya, 1967), grain size effects (Bunshah and Armstrong, 1969), effects of thermomechanical treatment (Chakin et al., 2007; Hill and Jones, 1961) and effects of neutron irradiation (Chakin et al., 2007). Like many hcp metals, beryllium is a highly anisotropic material (D. Webster, 2012; Walsh, 2009) and has a significant difference between the critical resolved shear stresses for basal slip (the primary slip system at room temperature) and other deformation modes (D. Webster, 2012). Indentation can be used for investigating mechanical anisotropy (Brookes et al., 1971; Hirsch et al., 1985), as has been demonstrated by experiments in monocrystalline beryllium, where indentation hardness with the indentation direction parallel to the [0001] direction was 2.2 - 2.8 times higher than for indentation perpendicular to [0001] as demonstrated by (Tsuya, 1967) and (Hill and Jones, 1961). Previous experiments (Hill and Jones, 1961; Tsuya, 1967) showed that indentation hardness coupled with crystallographic data is a useful approach for comparing the effects of different treatments on beryllium. For example, Tsuya (Tsuya, 1967) investigated the effect of temperature on the hardness of beryllium and demonstrated that while the Vickers hardness of the (0001) plane was higher than the $(10\bar{1}0)$ and $(11\bar{2}0)$ planes in the temperature range between 20 and 400°C; the relationship between hardness and surface orientation was independent of temperature. The lengths of the two diagonals of the Vickers impressions in $(10\bar{1}0)$ and $(11\bar{2}0)$ planes did change with temperature, which the authors linked to the alteration of predominant slip systems. The results of Hill

and Jones (Hill and Jones, 1961) showed that work hardening of beryllium single crystals led to highly non-uniform increase of hardness: ~30% for basal plane indentations but more than 3 times higher for indentations on prismatic planes.

Modern industrial beryllium grades are polycrystalline materials and modern fabrication methods allow production of fine-grained beryllium grades with a random distribution of crystallographic grain orientations (*Design Guides for Materion Beryllium Metal*, 2017), resulting in macroscopically isotropic properties. The average grain size of structural and nuclear grades typically does not exceed 20 μm (“S-65 Nuclear Grade Beryllium - Materion,” 2018, “S-200-F - Materion,” 2018, “S-200-F H - Materion,” 2018), too small for typical indentation sizes used for macro- and micro-hardness investigations. To study grain-specific response to indentation, only very small loads, which result in indentation depths at the nano-scale, and indentation widths less than ~10% of the grain size should be applied. The current work applies nanoindentation to investigate the response of grains with different crystallographic orientations during indentation. Several beryllium grades with different chemistry, grain size and texture were compared. Crystal plasticity (CPFEM) simulations were used to help interpret the nanoindentation results and to help mitigate against artefacts of the experimental technique.

2 Materials and techniques

2.1 Materials

The materials investigated in this work were four industrial beryllium grades:

1. S-65 high purity (Be > 99.2%) vacuum hot pressed nuclear grade (“S-65 Nuclear Grade Beryllium - Materion,” 2018);
2. PF-60 grade, which is also of high-purity (Be > 99.0%) but manufactured by hot pressing and hot-rolling and typically used for X-ray and particle-beam windows (“PF-60 Beryllium Foil for X-ray,” 2018);
3. less pure (Be > 98.5%) vacuum hot pressed S-200-F (“S-200-F - Materion,” 2018);

4. hot isostatically pressed structural grade S-200-FH (“S-200-F H - Materion,” 2018).

2.2 Techniques

Suitable surface conditions for nanoindentation and SEM/EBSD analysis were obtained by sequential mechanical grinding and polishing with SiC paper, diamond paste and colloidal silica. After mechanical polishing for SEM contrast increase, some areas were cleaned with the gallium ion beam in the dual beam SEM in the Materials Research Facility of the UKAEA using a FEI Helios FIB system dedicated for use with radioactive and toxic materials. During this step, the ion beam exposed an area of about $600 \times 350 \mu\text{m}^2$ in imaging mode perpendicularly to the surface, with energy of 30keV and current of 2 μA . About 5 minutes of the cleaning allowed clearer identification of grains, pores and precipitates in the secondary electron detector. Areas for indentation were not exposed to the gallium beam.

Indentations were conducted on a Keysight G200 nanoindentation system, with a three-sided diamond pyramid Berkovich tip, using the continuous stiffness measurement (CSM) technique (Oliver and Pharr, 1992) with a 42 Hz and 2 nm oscillation. The indenter tip was calibrated in fused silica to determine the contact area as a function of indenter displacement into the surface. The scanning mode of the G200 indenter was used to investigate the topography of the prints after indentation. The surface profiles were then extracted to correct the contact area due to pile-ups and sink-ins around the indent using open source software Gwyddion (“Gwyddion – Applications - <http://gwyddion.net/>,” 2018).

To quantify nanoindentation hardness H and indentation modulus E , the method used as a first approach was the now-standard method proposed by Oliver and Pharr (Oliver and Pharr, 1992) which forms the basis of the indentation testing standard (“ISO 14577-1,” 2015). The following equations were used:

$$H = \frac{P}{A} \quad (1)$$

$$E = \frac{1 - \nu^2}{\frac{1}{E^{eff}} - \frac{1 - \nu_i^2}{E_i}} \quad (2)$$

$$E^{eff} = \frac{S\sqrt{\pi}}{2\beta\sqrt{A}} \quad (3)$$

where A is the projected contact area of the indentation at load P , ν is Poisson's ratio of the test piece, 0.05 for beryllium (D. Webster, 2012), ν_i is Poisson's ratio of the indenter, 0.07 for diamond (“ISO 14577-1,” 2015), E^{eff} is the effective modulus of the contact between the indenter and the sample, E_i is the modulus of the indenter, 1140 GPa for diamond (“ISO 14577-1,” 2015), S is the contact stiffness, which is computed as the slope of the unloading curve continuously evaluated in the CSM mode, and β is the tip geometry correction factor (1.034 for a Berkovich tip) (Fischer-Cripps, 2004).

In this study, the standard Oliver-Pharr algorithm for nanoindentation data treatment was modified in order to take into account the influence of the plastic deformation on the sample surface around indents during loading, by which the contact area is modified from that calculated via the Oliver-Pharr algorithm. Both the “Oliver-Pharr” and the corrected area values were used in equations (1) and (3) and the results are compared in section 3.2.5. In this paper H_{O-P} , A_{O-P} and E_{O-P} refer to data obtained with the Oliver-Pharr algorithm, whereas H_C , A_C and E_C – are values after the contact area correction.

At least 200 indents were made for each beryllium grade with a target maximum indentation depth of 400 nm. Surface position correction was made for each indentation before data analysis. For consistency, load and contact stiffness data averaged between 320 and 360 nm indentation depth were used for indentation hardness and modulus calculations, avoiding the depth range within which there is a strong indentation size effect. In order to investigate the crystallographic dependence of nanoindentation hardness, EBSD analyses of the indentation arrays were made, using a JEOL 840A scanning electron microscope equipped with the EDAX-TSL EBSD; OIM TSL software (“OIM AnalysisTM/ EDAX,” 2018) was used for analysis of the EBSD data. Surface normal-projected inverse pole figure orientation maps superimposed with image quality (a parameter quantifying the quality of

the corresponding diffraction pattern (Wardle et al., 1994)) maps were used for indent localisation. Data from indents covering grain boundaries and in close proximity to them were analysed separately and were not considered in the crystallographic orientation analyses.

2.3 Crystal Plasticity Finite Element Method (CPFEM)

Finite element simulations using Abaqus 2016 (Abaqus (2015) ‘Abaqus 2016 Documentation’, 2016) were performed to investigate the influence of crystallographic orientation of the indented beryllium grain on the mechanical response. Simulations provided load as a function of indentation depth and details of the plastic deformation of the free surface around indents; deformation affects the contact area between the tip and the sample and hence the accuracy of the hardness and elastic modulus. A strain gradient crystal plasticity user material (UMAT) for Abaqus was developed based on the user element (UEL) written by Dunne and Kiwanuka (Dunne et al., 2012, 2007). To allow the curl of the plastic deformation gradient to be calculated within a UMAT, the initial Gauss point coordinates and current value of the plastic deformation gradient F^p at every integration point were stored in a common block; this was protected using the Abaqus utility subroutine `MutexLock()` to enable parallelisation. A total of 193,800 (C3D8) Abaqus linear elements with full integration (8 Gauss points/element) were used to represent a cube with dimension of $L = 40 \mu\text{m}$. The computational cost of linear elements was significantly less than quadratic elements, which allowed a very fine biased mesh under the indent to be used: $w = 50 \text{ nm}$, increasing up to $w = 2 \mu\text{m}$ away from the indent. The indenter tip was modelled as a rigid object with a perfect Berkovich geometry. The small sliding, node to surface, Abaqus contact algorithm was used with the default frictionless hard contact property. The top (blue) surface was traction-free while the remaining 5 (red) surfaces were fixed as shown in Figure 1 (c).

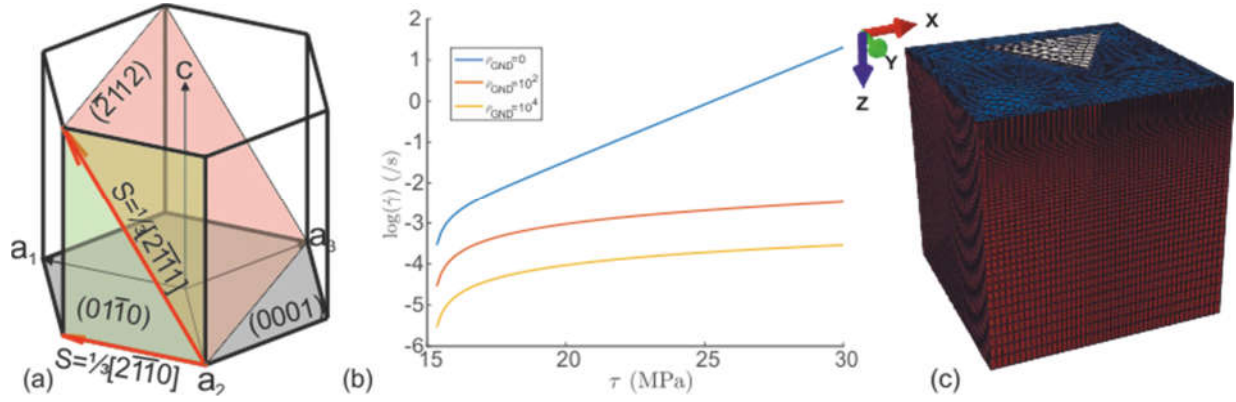


Figure 1. a) the $\langle a \rangle$ basal, $\langle a \rangle$ prismatic and secondary $\langle c+a \rangle$ slip systems. (b) The slip rate on the $\langle a \rangle$ basal systems for different GND densities. As the GND density increases the slip rate decreases for a given stress due to GNDs acting as obstacles to dislocation slip. (c) The FE mesh.

Elastic anisotropy was used with the following elastic constants $E_1 = E_2 = 289$ GPa, $E_3 = 335$ GPa, $G_{12} = 138$ GPa, $G_{13} = G_{23} = 162$ GPa and $\nu_{12} = 0.09$, $\nu_{13} = \nu_{23} = 0.04$; these correspond to $c_{11} = c_{22} = 292.3$ GPa, $c_{33} = 336$ GPa, $c_{44} = 132.8$ GPa, $c_{55} = c_{66} = 162.5$, $c_{12} = 26.7$ GPa, $c_{13} = c_{23} = 12.8$ GPa (Knezevic et al., 2013; Walsh, 2009). The 3 $\langle a \rangle$ basal, 3 $\langle a \rangle$ prismatic and 6 $\langle c+a \rangle$ secondary pyramidal slip systems, see Figure 1(a), were included with a constant CRSS of $\tau_c = 15$ MPa for the $\langle a \rangle$ basal, $\tau_c = 68$ MPa for the $\langle a \rangle$ prismatic systems, and $\tau_c = 2000$ MPa for the secondary $\langle c+a \rangle$ pyramidal systems. These values were taken from the literature (Knezevic et al., 2013; Walsh, 2009). Simulations were performed for several crystal orientations of the indented surface, to probe the “hard” and “soft” orientations.

The total deformation \mathbf{F} is decomposed multiplicatively into plastic (\mathbf{F}^p) and elastic (\mathbf{F}^e) deformation gradients:

$$\mathbf{F} = \mathbf{F}^e \mathbf{F}^p \quad (4)$$

where the flow rule has the form

$$\dot{\mathbf{F}}^p = \mathbf{L}^p \mathbf{F}^p \quad (5)$$

The plastic velocity gradient, \mathbf{L}^p , is given by the crystallographic strain rate resulting from dislocation glide on the active slip systems with slip direction \mathbf{s}^α and slip plane normal \mathbf{n}^α

$$\mathbf{L}^p = \sum_{\alpha} \dot{\gamma}^{\alpha} (\mathbf{s}^{\alpha} \otimes \mathbf{n}^{\alpha}) \quad (6)$$

The crystallographic slip rate on slip system α is $\dot{\gamma}^{\alpha}$ given by (Dunne et al., 2012, 2007)

$$\dot{\gamma}^{\alpha} = A \sinh((\tau^{\alpha} - \tau_c) V / kT) \quad (7)$$

where the prefactor $A = 3 \times 10^{-3} / s$ for $\langle a \rangle$ slip and $A = 1 \times 10^{-2} / s$ for $\langle c+a \rangle$ was treated here as a fitting parameter, although it can be related to the physically based constants $A = \rho_m b^2 f \exp(-\Delta F / kT)$, implying a mobile dislocation density ($\rho_m = 3 \times 10^{-3} / \mu m^2$), attempt frequency ($f = 10^{11} / s$) Helmholtz free energy ($\Delta F = 3.46 \times 10^{-8}$ pJ) and Burgers vector length $b = 0.228$ nm for $\langle a \rangle$ slip and 0.424 nm for $\langle c+a \rangle$. The activation volume was assumed to be $V = B b^2 / \sqrt{\rho_0 + \rho_{GND}}$ where c is a dimensionless fitting parameter ($B = 0.05$) and ρ_0 an initial sessile dislocation density (assumed to be $1 / \mu m^2$) required to ensure a finite strain in the absence of GNDs. Minimal fitting was performed: A and B were calibrated using one load displacement curve only; all other parameters were from literature. Hardening occurs through the activation volume parameter V (see Figure 1(b)) which was assumed to be proportional to the total (edge + screw) GND spacing. A total of 12 slip systems was included in the model giving a possible 12 edge + 9 screw dislocation types. Only the total scalar density was used in the slip law which was obtained by summing the absolute values of all 21 densities, $\rho_{GND} = \sum_{\alpha=1}^{\alpha=21} |\rho^{\alpha}|$. The 21 densities were found by reformatting the Nye-Kröner-Bilby tensor into a set of linear equations

$$\mathbf{M}_{i\alpha} \rho_{\alpha} = G_i \quad (8)$$

where column α of \mathbf{M} is the tensor product $\mathbf{l}^{\alpha} \otimes \mathbf{b}^{\alpha}$ of the dislocation line direction and Burgers vector of slip system α , reshaped as a column vector, and the RHS is

$$G_{km} = \text{CURL}(\mathbf{F}^p)_{km} = \varepsilon_{ijk} \partial F_{mj}^p / \partial X_i \quad (9)$$

also reshaped as a column vector (Arsenlis and Parks, 1999). Note that the reshaping of $\mathbf{l}^\alpha \otimes \mathbf{b}^\alpha$ and G_{km} into column vectors can be done row-wise or column-wise provided it is done consistently on both sides of equation (8). As \mathbf{M} is not square (having 9 rows and 21 columns) it cannot be inverted; instead the pseudo right inverse was found

$$\mathbf{M}^{-r} = \mathbf{M}^T (\mathbf{M}\mathbf{M}^T)^{-1}, \quad M_{i\alpha} M_{\alpha j}^{-r} = \delta_{ij}, \quad (10)$$

which allows the L^2 minimum solution for the GND density on each slip system, ρ_α , to be obtained for every possible slip system

$$\rho_\alpha = M_{\alpha j}^{-r} G_j \quad (11)$$

The resulting crystallographic slip rate is shown in Figure 1 for different values of ρ_{GND} . It should be noted that twinning, which is known to be an important deformation mechanism in beryllium crystals under compression (Brown et al., 2012; D. Webster, 2012) was not incorporated in the current crystal plasticity model.

3 Results and discussion

3.1 Microstructure

Figure 2 shows a comparison of the microstructures of the investigated beryllium grades. The white contrast objects on the micrograph are precipitates, typically enriched with oxygen, aluminium, iron, silicon, titanium and other impurities, as was demonstrated by our previous STEM/EDS studies of beryllium (Kuksenko et al., 2017). There is a noticeable difference between grades which is likely to have originated from the different thermomechanical treatment histories of the grades: in the hot rolled PF-60 grade precipitates are mainly located in small, often elongated agglomerates inside grains, whereas in the grades produced by VHP and HIP the precipitates are mainly at grain boundaries.

Grains mainly have irregular but roughly equiaxed shapes, containing some thin elongated twins. In this study the twins were not quantified, but from the visual inspection (see Figure 2) it is clear that the HIP-ed S-200-FH grade has a significantly larger number density of twinned grains.

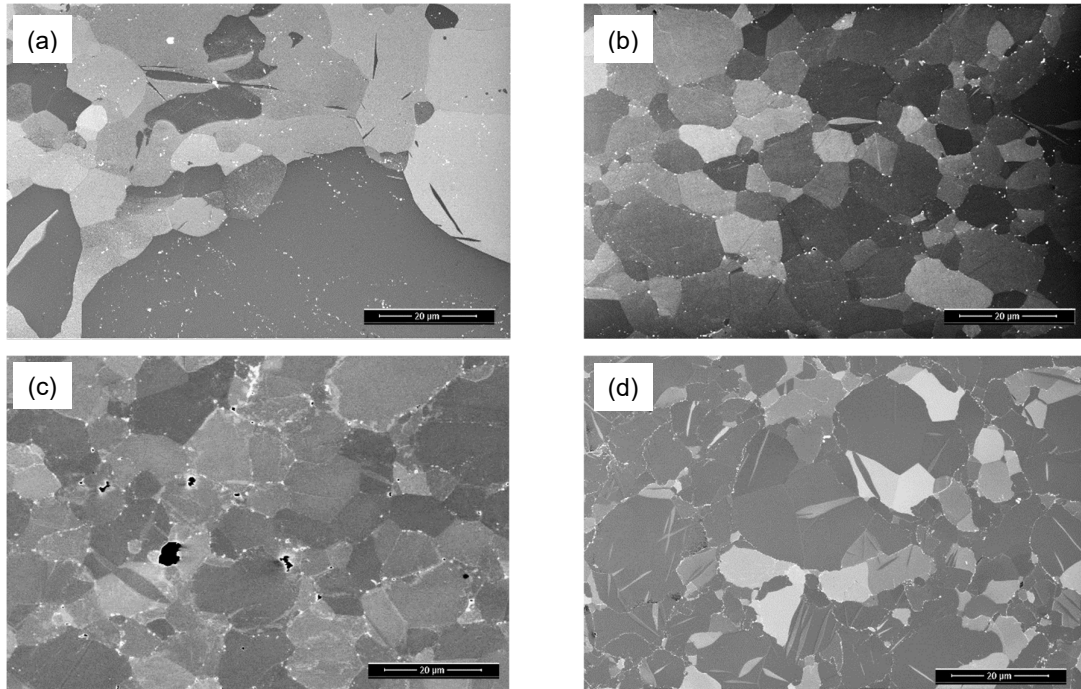


Figure 2. SEM (secondary electron) images of the beryllium grades tested: (a) PF-60 – hot-rolled, (b) S65 – vacuum hot pressed, (c) S200F – vacuum hot pressed and (d) S200FH – hot isostatically pressed grades. Impurity precipitates are visible as white objects while pores are black.

Figure 3 shows EBSD maps from the areas of the nanoindentation arrays; the normal-projected inverse pole figure orientation maps (in colour) are superimposed on the image quality maps (Wardle et al., 1994) (in grey). Dark areas indicate low EBSD image quality and correspond to grain and sub-grain boundaries, and areas around nanoindentations. The SEM micrographs and EBSD maps demonstrate that each of the investigated grades has a considerable variation of grain size. PH-60 grade has noticeably larger grains than the other investigated grades. Average grain diameter measured from the EBSD maps is $(25 \pm 14) \mu\text{m}$ for the hot-rolled grade, $(7.3 \pm 4.4) \mu\text{m}$ in the S-65, (7.1 ± 4.1) in the S-200-F grade and $(5.3 \pm 3.3) \mu\text{m}$ for the HIP-ed S-200-FH grade. Note that since the step size for the EBSD mapping was from 0.4 to 0.6 μm , very thin twins were not taken into account during the grain-size calculations.

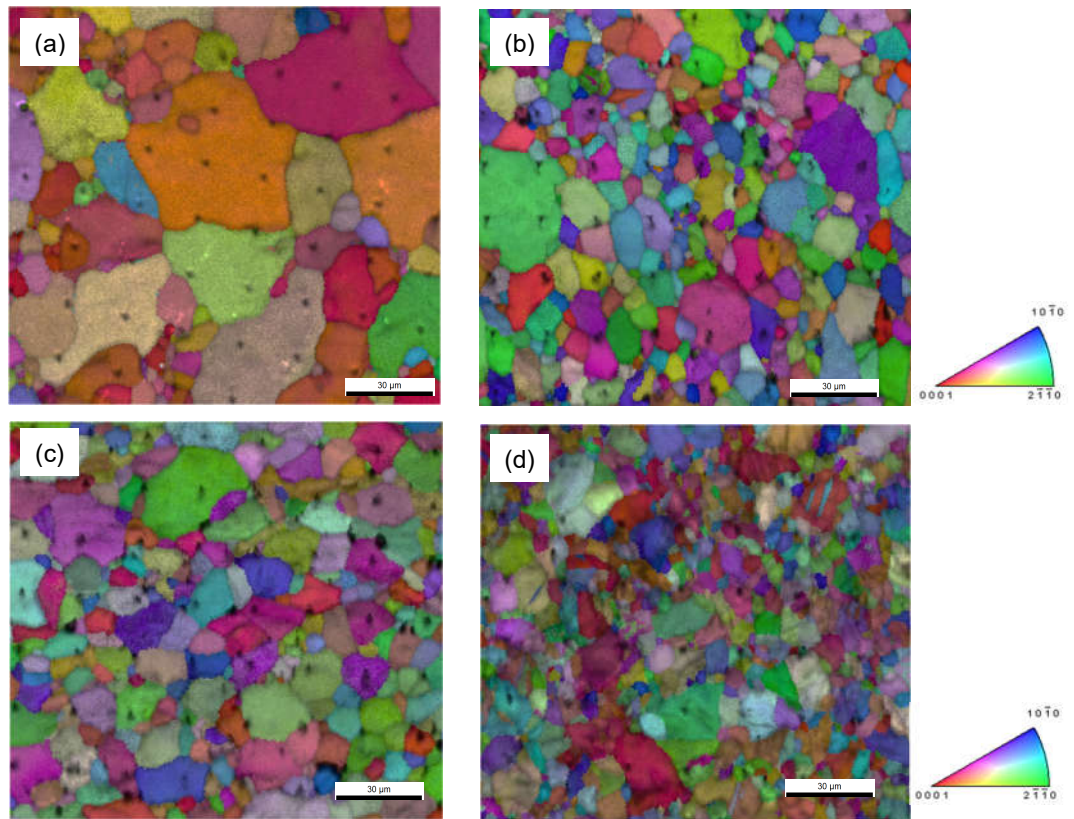


Figure 3. Surface normal-projected inverse pole figure orientation maps (in colour) superposed on image quality maps (Wardle et al., 1994) (in grey) for the PF-60 (a), S65 (b), S200-F (c) and S-200-FH(d) grades. Dark areas indicate a low EBSD image quality and correspond to grain and sub-grain boundaries, and to areas of indentation impressions.

The EBSD inverse pole image in Figure 3(a) shows that the PF-60 hot rolled beryllium grade has a crystallographic texture with a preferential orientation of the basal plane (0001) close to the plane of observation. This texture results from the hot rolling used for forming the PF-60 sheet (“PF-60 Beryllium Foil for X-ray,” 2018). The other beryllium grades investigated do not have any noticeable texture.

3.2 Nanoindentation data

3.2.1 Load vs displacement data analysis

Figure 4 (a) shows the averaged load on each sample as a function of indentation depth. These plots do not include indents into grain-boundaries. The average load needed for indentation to the same depth is higher for the PF-60 grade than for the HIPed and the VHP grades. Significant scatter around the average values was observed in all of the beryllium grades investigated as demonstrated by the standard deviation error bars in Figure 4(a). Different possible origins of this scattering were assessed and the crystallographic orientation of the indented grain appears to be the most dominant. Figure 4(b) shows the load-displacement data for the PF-60 grade (the blue data points in Figure 4(a)) grouped according to the angle between the indentation direction and the [0001] axis of the indented grain (which for the remainder of this paper is denoted θ); each sub-dataset covers a 15° range. Indentations 400 nm deep into the basal plane (i.e. with small θ) require about 17 mN, almost twice as high a load as for indentation into surface planes perpendicular to the [0001] axis (i.e. $\theta \sim 90^\circ$). The standard deviation for each sub-dataset (typically ± 2.4 mN, at 380nm depth) is significantly smaller than for the whole dataset covering all orientations of non-grain-boundary indentations (typically ± 0.6 mN, at 380nm depth).

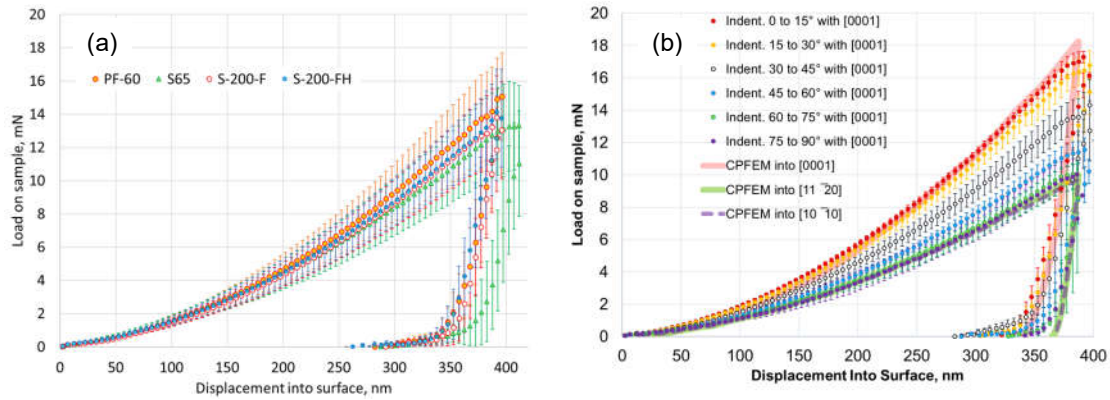


Figure 4. (a) Load as a function penetration of the indenter tip into the surface in 4 industrial beryllium grades. (b) Load as a function of penetration of the indenter tip into surface of the PF-60 grade beryllium sample split depending on the crystal orientation of the indented grain. Experimental results are compared with CPFEM data for indentation into surfaces normal to three crystallographic orientations: [0001] parallel to the c-axis ($\theta = 0$) and orthogonal to it ($\theta = 90$) along $\langle 10\bar{1}0 \rangle$ and $\langle 11\bar{2}0 \rangle$. Error bars correspond to the standard deviation of the load around the average value.

The indentations made in three crystallographic directions were also simulated with CPFEM. The simulated load displacement curves for indentations into “hard” [0001] ($\theta = 0$) and “soft” $[10\bar{1}0]$ and $[11\bar{2}0]$ crystallographic directions ($\theta = 90$) (i.e. into surfaces normal to these directions) are shown in Figure 4(b) as wide pink, green and dashed purple lines. The two free parameters in the slip law, the slip rate prefactor A and the hardening parameter B , relating GND density to activation volume, were calibrated to reproduce the load displacement curve in the [0001] orientation, with all other parameters taken from the literature. These parameters were then used for simulation of indentations in the $[10\bar{1}0]$ and $[11\bar{2}0]$ directions. The excellent agreement between experimental data and modelling for the two soft orientations implies that the CRSS values and slip law are reasonable and confirms that the origin of the experimentally observed scatter in nanoindentation results in these polycrystalline materials is anisotropy in the plastic slip from indentations into differently-orientated grains..

3.2.2 GND density and elastic fields

Figure 5(a) – (c) shows CPFEM contour plots of the total geometrically-necessary dislocation (GND) density, ρ_{GND} , on a log scale, at maximum load for indentations in the “hard” and the two “soft” orientations. The majority of GNDs are produced in a localized area just under the indent (yellow, orange and red zones on Figure 5). In the hard orientation the region of high GND density is predicted to penetrate further into the sample than for the soft orientations. Easy $\langle a \rangle$ slip on basal and prismatic planes produces lobes of high plastic strain and hence high GND density in the 3 $\langle a \rangle$ directions and in the 3 directions made up of the combinations of two different $\langle a \rangle$ directions. This is shown in Figure 5c where the soft orientation (indentation into a prismatic plane parallel to the free surface) produces a GND density pattern reflecting slip plane orientations when viewed down the c-axis.

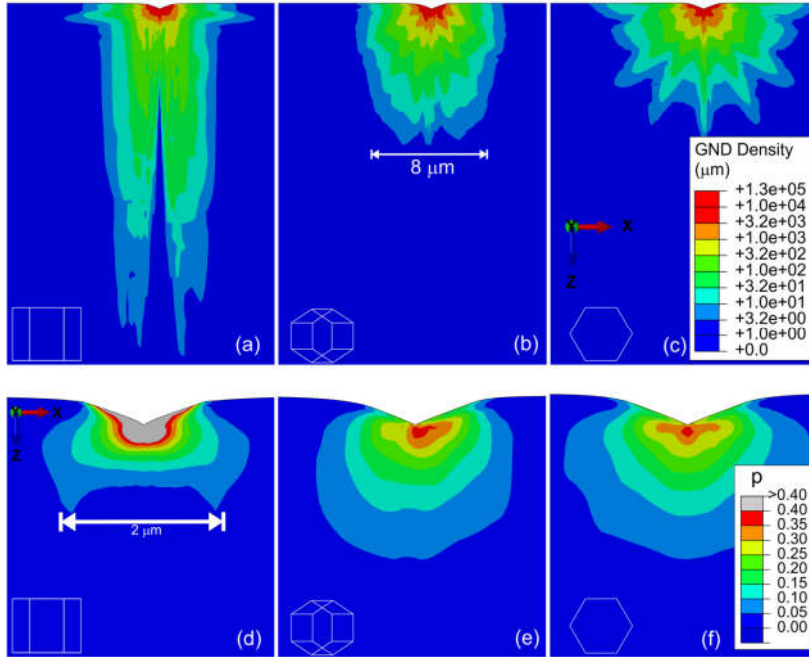


Figure 5 . The total GND density (log scale) at maximum load (surface penetration depth of 387 nm) for indentations in the hard [0001] (a) and two soft orientations [11 $\bar{2}$ 0] (b) and [10 $\bar{1}$ 0] (c) on the plane $y = 0$ which slices through the center of the simulated cube directly under the indent. The corresponding effective plastic strain (linear scale) in an enlarged section under the indent is shown in (d, e, f) and is mainly localised in a volume size ~ 7 times larger than the indentation depth. The scale bar shown in (b) is applicable for (a) and (c), while the scale in (d) is applicable to (e) and (f).

Figure 5(d)–(f) shows the effective plastic strain at maximum load for simulations of indentations made in the 3 different crystallographic orientations. The plastic strain is highly localized near the indent, and therefore only a smaller region of material is shown than in Figure 5(a)-(c). The maximum plastic strain value is greatest ($>40\%$) for the hard orientation directly under the indent. Field plots at different depths showed that the plastic zone depth and surface extent, defined by the volume with an effective plastic strain greater than 5%, was approximately 7 times larger than the tip penetration depth. This suggests that if the surface distance between the indent and the nearest sub-surface grain boundary is more than 8 times the indentation depth, then plastic response of the material will be that for a single crystal of the chosen crystallographic orientation. This approach was used in the current work to remove grain-boundary indentation data from single crystal data. Since it is not possible to determine

grain structure in volumes under the surface cross-section, the approach naturally suffers from scattering generated by the possible presence of grains with different orientation in close proximity under the surface cross-section.

Figure 6 shows the predicted four in-plane components of the elastic stress tensor on the $y = 0$ plane directly under the indent for the hard $[0001]$ and soft $[10\bar{1}0]$ orientations at maximum load. Figure 6(a) and (c) show that the soft orientation has a larger volume of material with a compressive σ_{xx} , whereas the σ_{zz} component of stress for the hard orientation penetrates very deep into the material compared to the soft orientation. The easy $\langle a \rangle$ slip in the soft orientation also reduces the elastic stress and hence reaction force, in good agreement with the measured load-displacement curves, as shown in Figure 4 (b). The simulation results demonstrate that the field of significant elastic interaction between the indenter tip and beryllium samples is almost two orders of magnitude larger than the tip penetration depth and thus for the ~ 400 nm deep indents used here it extends up to ~ 40 μm from the indented surface. This is significantly larger than the average grain radius of the tested beryllium grades (from 2.7 to 12.5 μm).

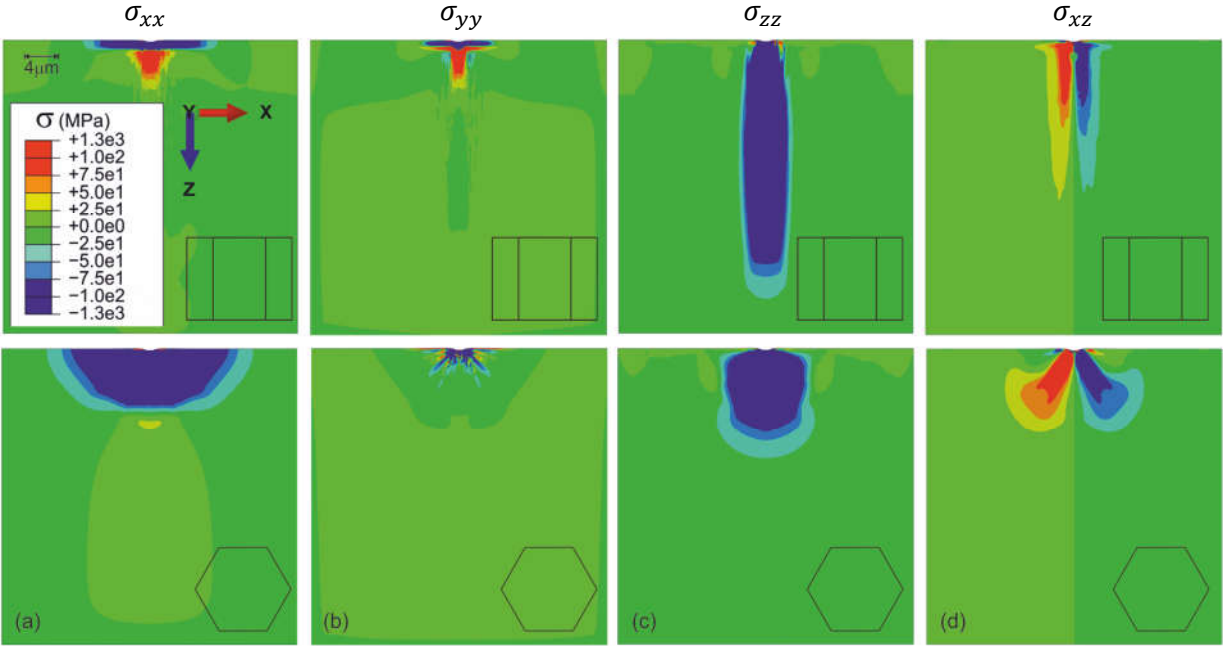


Figure 6. The in plane elastic stresses under the indent for the hard and soft orientation at maximum load (a) σ_{xx} , (b) σ_{yy} , (c) σ_{zz} and (d) σ_{xz} . Upper row corresponds to the indentation into “hard” [0001] orientation ($\theta = 0$), lower row demonstrates the indentation into “soft” $[10\bar{1}0]$ direction ($\theta = 90^\circ$).

3.2.3 Contact area

In order to calculate accurate hardness values, the contact area between the indenter and the sample in equation (1) should be correctly determined. In the standard method proposed by Oliver and Pharr (Oliver and Pharr, 1992) the contact area used in equations (1) and (3) for hardness and modulus calculation is determined from the tip area function $A(h_c)$ that expresses the indenter’s cross-section area in terms of the contact depth, h_c . The contact depth, $h_c = h_{max} - h_s$, is the difference between the measured total penetration of the tip into the surface, h_{max} , and the elastic surface displacement, h_s . The elastic displacement, $h_s = \varepsilon \frac{P_{max}}{S}$, is calculated using the Oliver-Pharr model (Oliver and Pharr, 1992) where P_{max} is the measured maximum load, S is the elastic unloading stiffness and ε is the Berkovich tip geometry coefficient. However it is known that elastic, plastic and strain-hardening properties of a material can affect its behaviour underneath the indenter tip and the material may either plastically sink-in or pile-up around the indenter (Bolshakov and Pharr, 1998; Fischer-Cripps, 2004;

McElhaney et al., 1998). Both piling-up and sinking-in may significantly change the contact area between the indenter tip and surface (see examples from tungsten (Beck et al., 2017), copper (McElhaney et al., 1998), titanium (Britton et al., 2010; Su et al., 2016; Zambaldi et al., 2012), nickel (Renner et al., 2016) and iron-based alloys (Hardie et al., 2015)). If unaccounted for, the calculated indentation hardness and modulus would be too high if pile-up occurs (as the real contact area is greater than that calculated from the indenter profile and penetration depth) and too low when sink-in occurs (when the real contact area will be less than the calculated one).

In order to estimate the out-of-plane plastic deformation of beryllium and hence to improve the analysis of the load-displacement data to give indentation hardness, direct imaging of the residual impressions, using indenter scanning under a low contact load (1 μN), was performed for 47 indents covering a range of indentation orientations for the 4 grades studied. Figure 7 shows examples of experimentally measured topography maps around indents into 3 different grain orientations and CPFEM simulations for similar indentation orientations. For all indentations, plastically deformed surface zones were observed well outside the area of the tip penetration.

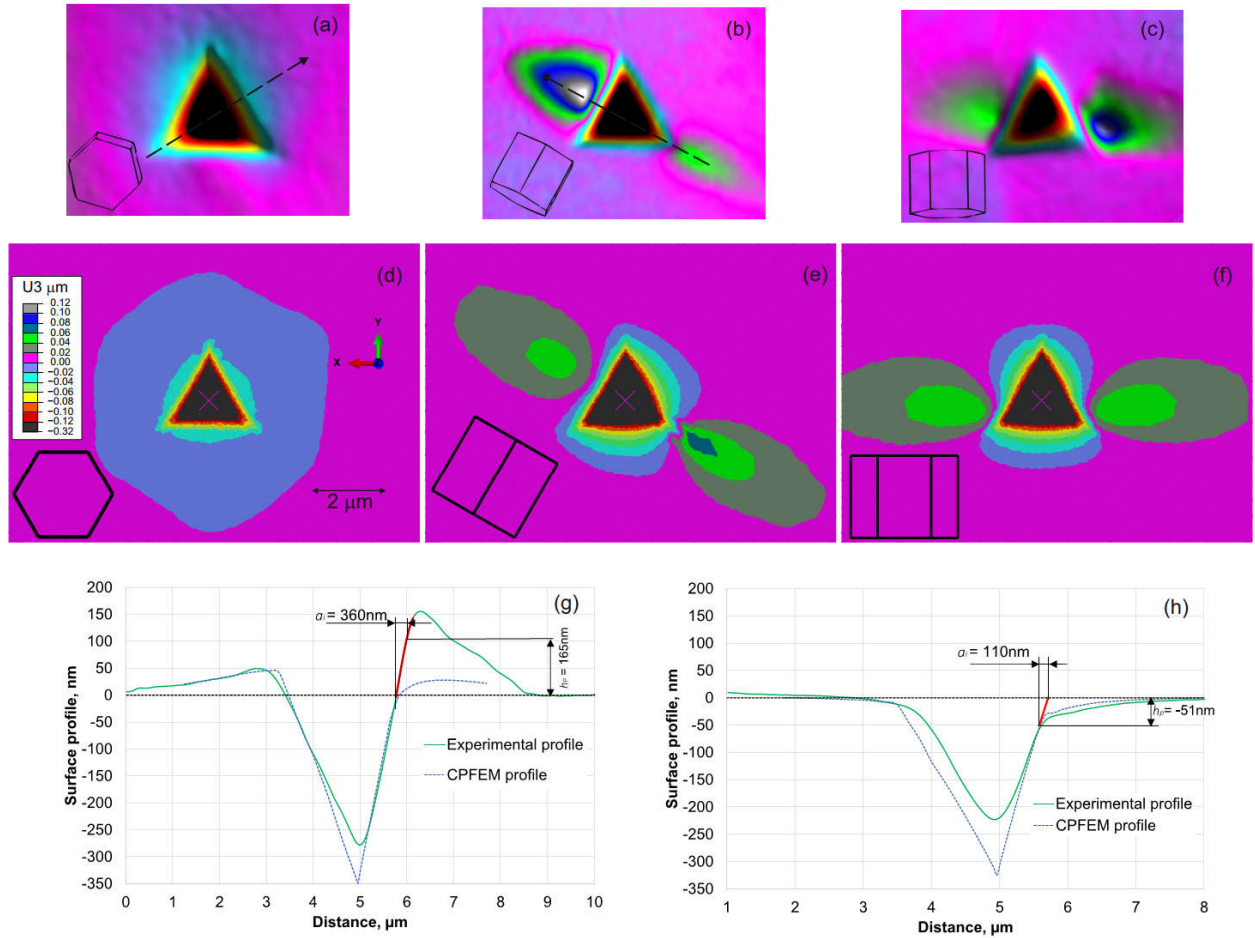


Figure 7. Examples of 400 nm indents. PF-60 HR beryllium. (a) – (c) topography maps scanned with the nanoindenter tip. The inset hexagon prisms indicate the crystallographic orientation of the indents. The angle between indentation direction and the [0001] axis, θ , is (a) 6° , (b) 82° , (c) 81° with. (d) – (f) showing the corresponding topography maps obtained by CPFEM. The same colour contour scale is used in (a)–(f). In the hard orientation sink-in occurs reducing the contact area; whereas in the both soft orientations pile-up occurs increasing it. Parts (g) and (h) show examples of experimentally-determined indent print profiles corresponding to the arrows on (b) and (a), demonstrating pile-up (g) and sink-in (h).

Estimations of the real contact areas were made using the approach proposed by Kese et al (Kese et al., 2005). The method requires experimental measurement of the indent profile through the central point of indentation and the centre of each edge, as shown in Figure 7(a) and (b). Where pile-up is observed, Figure 7(g), the contact between the indent and the pile-up is determined and is then projected onto the direction of the free surface normal, giving the pile-up height, h_p . The contact area

of each pile-up is then approximated as a semi-ellipse, with the major axis equal to the length of the side of the projected triangular area of the indent print, and the minor axis being measured on the indent profile image as the projected distance of the pile-up contact perimeter as demonstrated in Figure 7(g). Originally, Kese et al (Kese et al., 2005) proposed the method for estimation of pile-up contribution only, however, in this work, the approach was modified to account for the observed sink-ins: the reduction in contact area was also approximated as a semi-ellipse, with a major axis calculated in the same way, whereas the minor axis was measured on the indent profile image as the projected distance between the sink-in contact perimeter as shown in Figure 7(h). For each investigated indent the corrected projected area, A_{corr} , was calculated as the contact area determined by the Oliver–Pharr analysis (Oliver and Pharr, 1992), $A_{\text{O-P}}$ plus (or minus) the area due to out-of-plane deformation near each edge for pile-ups (or sink-ins).

Figure 8(a) shows the magnitude of the out of plane plastic deformation for all the measured profiles, where 3 data-points across each edge of the investigated indent print were sorted from the smallest value (blue data points) to largest (red data points). The graphs show that, for all indentation directions, both pile-ups and sink-ins are simultaneously present in the vast majority of indentations. For indentation with $\theta < 15^\circ$ (hard orientations), at least two edges had adjoined sink-ins whereas the third edge had either sink-in or small pile-up. The residual sink-in area was spread out up to $\sim 1.5\mu\text{m}$ around the indent, as shown by the blue “halo” around the indenter print on Figure 7(a) with the maximum depth up to $\sim 55\text{ nm}$. The simulated residual out of plane displacement from the crystal plasticity model (Figure 7(d)) qualitatively corresponds to the experimentally observed behaviour; however the predicted deformed area was more symmetric than found in experiments. For indentations with $\theta \sim 90^\circ$ (soft orientations), pile-up dominated and exhibited two hills on opposite sides of the indentation pit. The pile-up maxima are aligned with the traces of the $\langle a \rangle$ directions onto the free surface. Depending on the orientation of the indenter tip two types of pattern were observed:

- i) If the c-axis of the grain was approximately perpendicular to one of the edges of the tip, this edge typically exhibited sink-in, and pile-up occurred at the other two edges (see Figure 7(c)).
- ii) If one of the tip's edges was approximately parallel with the c-axis of the indented grain, then one large pile-up (up to 220nm height) was observed near this edge, and the second pile-up was near the opposite corner of the indentation tip (see Figure 7(b)). This type of pile-up was not detected by profile measurements through the centres of the neighbouring edges, where small sink-ins were typically observed.

The pile-up patterns described above were very pronounced for indentations close to the hard and soft orientations shown in Figure 8 but more complicated behaviour was observed for intermediate angles. The additional contact depth due to pile-ups was less than 50 nm for indentation angles up to about 40° and then became more pronounced reaching a maximum of approximately 185 nm for orientations near 90°, as demonstrated in Figure 7(b).

Pile-ups predicted by CPFEM simulations had a shape and position consistent with experimentally observed patterns although the maximum heights of the observed hills were smaller than in experiments and reached only 50 nm. This difference could be due to constraint from nearby crystals in the real sample enhancing the pile-up; when the dimensions of the simulated cube were halved the simulated pile-up profile was found to approximately double. Alternatively (or additionally) this discrepancy could be due to the approximations and simplifications made in the slip law. CPFEM was also able to predict sink-in behaviour for indentations away from the [0001] direction; however, the sink-in size observed in simulations was larger than the experimentally measured values.

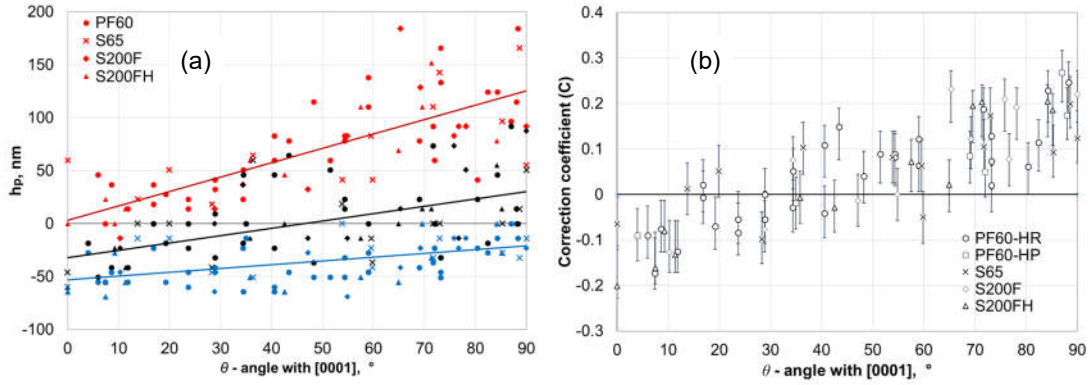


Figure 8. Distribution of the surface plastic deformation contribution to contact depth (a) and the contact area correction coefficient (b) for different crystal orientations. Error bars – min and max values considering 30 nm uncertainty of the contact area edge determination.

Figure 8(b) shows changes in contact area between the indenter and the sample due to pile-ups and sink-ins, where the contact area correction coefficient, C , is shown as a function of indentation angle. C is calculated as:

$$C = \frac{A_{\text{corr}} - A_{0-P}}{A_{0-P}} \quad (12)$$

The sink-in behaviour dominates for indents into grains with surface normals oriented close to the c -axis, reducing the contact area. The corresponding correction coefficient was measured to be in the range of approximately -0.1 to -0.2. Pile-up dominates for indents into grains with surface normal oriented far away from [0001]. The correction coefficient gradually increases with indentation angle, reaching 0.25 for indents into grains with surface normal oriented perpendicular to [0001].

The averaged correction coefficient as a function of indentation angle θ between the c axis of the grain and the loading direction can be fitted to a linear function:

$$C = a_1\theta + a_0 \quad (13)$$

Coefficients $a_1=0.0035$ and $a_0=-0.123$ if the full data set is used (all beryllium grades, excluding indents close to grain boundaries), the coefficient of determination $R^2=0.72$. If the fitting $C = f(\theta)$ is done separately for the different beryllium grades, the less pure S-200-F and S-200-HF beryllium

grades have a larger a_1 coefficient (up to 0.043) and slightly smaller a_0 coefficient (−0.181) implying deeper sink-in deformations for the c-axis indents and a more pronounced trend towards pile-ups in soft orientations.

The sensitivity of pile-up/sink-in behaviour in beryllium to crystallography and indenter orientation as captured by the correction coefficients, C , in beryllium is in contrast to the behaviour observed in isotropic materials, where the susceptibility to piling-up or sinking-in and its contribution to indentation contact area at a specific indentation depth can be approximated as a constant parameter as, for example, proposed for strain-hardened and annealed states of FCC copper (McElhane et al., 1998). It is generally observed that a low (σ_y/E) ratio and the absence of strain-hardening both promote the formation of pile-ups whereas the converse leads to the creation of sink-ins (Bolshakov and Pharr, 1998; Fischer-Cripps, 2004). Because of the complex three-dimensional profile of the strain and stress fields under the 3-sided pyramidal indenter tip, it is difficult to compare different orientations of the same materials using a single scalar value for E , σ_y and the strain-hardening parameter. However the simulated stress field (Figure 6) and GND density map (Figure 5) penetrate deeper into the material in the hard orientation relative to the soft orientation consistent with a higher (σ_y/E) ratio; and the plastic strain under the indent is also higher (Figure 5) consistent with GND hardening.

3.2.4 Indentation-derived elastic modulus

The Young's modulus of industrial polycrystalline beryllium is around 303 GPa (Walsh, 2009). However, it is known that Young's modulus of beryllium is anisotropic and varies with crystallographic orientation from 341 GPa (parallel to [0001]) to 287 GPa (perpendicular to [0001]) (Walsh, 2009), as shown in Figure 9 by the blue line.

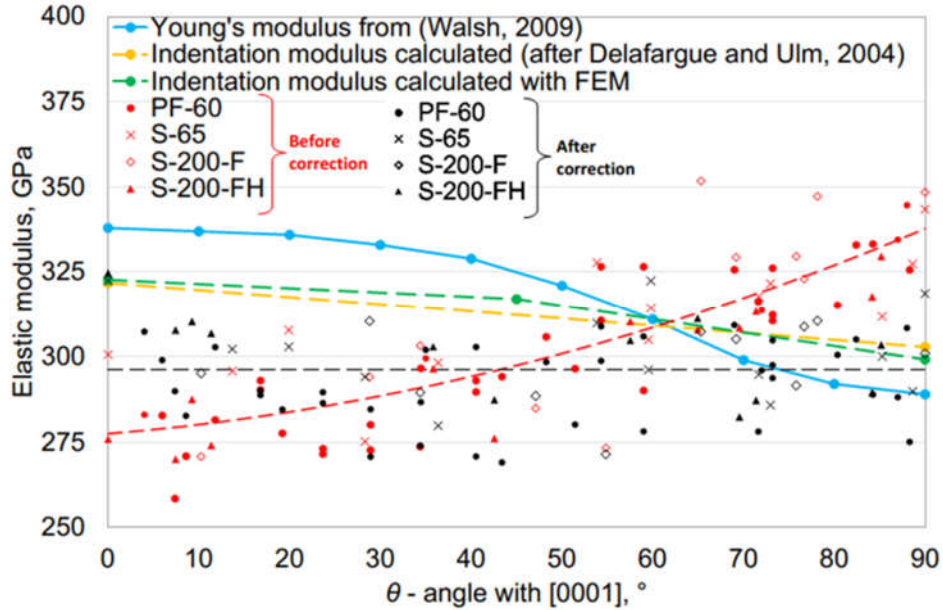


Figure 9. Comparison of elastic moduli with experimentally observed and calculated indentation moduli for different crystallographic orientations

Since the indentation modulus is obtained from a complex, three-dimensional, non-uniform stress state, the indentation modulus with indenter aligned along a given crystallographic direction usually differs significantly from the Young's modulus for uniaxial deformation in that direction (Haušild et al., 2014; Vlassak and Nix, 1994). An anisotropic elastic material law was also used to perform finite element simulations and the predicted beryllium indentation moduli for indentation angles of 0° , 45° and 90° were 330 GPa, 320 GPa and 303 GPa respectively (green dashed line in Figure 9). The analytical calculation of indentation moduli for monocrystals in the principal materials symmetry directions proposed by Delafargue and Ulm (Delafargue and Ulm, 2004), using anisotropic elastic constants from (Knezevic et al., 2013; Walsh, 2009), this indentation moduli were calculated to be about 321 GPa (0° to $[0001]$) and 302 GPa (90° to $[0001]$), as indicated by the yellow dashed line in Figure 9. The FEM predictions and the Delafargue and Ulm analytical solution are in good agreement with each other, and predict higher indentation moduli near the $[0001]$ direction ($\theta = 0$) relative to $[11\bar{2}0]$ and $[10\bar{1}0]$ directions ($\theta = 90^\circ$). However, the experimental indentation moduli extracted from the nanoindentation test data using the

Oliver-Pharr method, E_{O-P} , equations (2) and (3), show the reverse trend with indenter orientation ,increasing from ~275 GPa when $\theta = 0$ to ~340 GPa when $\theta = 90^\circ$ (red data and line in Figure 9).

The measured pile-up and sink-in contribution coefficient C estimated using topography mapping profilometry was used to correct the indentation modulus E_c using equation (14) derived from the combination of equations (2), (3) and (12):

$$E_c = \frac{1 - \nu^2}{\sqrt{C + 1} \left(\frac{1 - \nu^2}{E_{O-P}} + \frac{1 - \nu_i^2}{E_i} \right) - \frac{1 - \nu_i^2}{E_i}} \quad (14)$$

The corrected values (black points and line in Figure 9) gives an increase in calculated modulus values in indents where sink-in dominates ($\theta \sim 0^\circ$) and lowers the modulus when pile-up dominates ($\theta \sim 90^\circ$). The corrected moduli do not have any noticeable dependence on indentation angle for the investigated samples, and are scattered around the average value of 296 GPa. This is likely due to the assumption that only a single crystal was being probed during indentation, while during the experiment polycrystalline beryllium samples were tested. As demonstrated in Figure 6, the field of elastic interaction between the indenter tip and beryllium samples is almost two orders of magnitude larger than the indentation depth and was significantly larger than the average grain size of the tested samples. This implies that the elastic response which determines contact stiffness from equation (3) for the effective modulus calculation is averaged over many crystallographic orientations and only weakly depends on the orientation of the indented grain. The measured average modulus of 296 GPa is in good agreement with the Young's modulus of industrial polycrystalline beryllium, which is between 292 and 304 GPa when measured in the hot pressed S-200-E grade (Christman and Feistmann, F.J., 1972).

It is important to emphasise that while our experimentally measured indentation modulus, E_c , did not have a clear dependence on crystal orientation, the orientation did determine the localised plastic deformation and hence the contact area correction coefficient, C .

3.2.5 Hardness data

In this section, hardness values for all of the investigated grades will be extracted using the standard method (Oliver and Pharr, 1992) and accounting for the contact area correction. The measured pile-up and sink-in contribution coefficient C can be directly used for nanoindentation hardness correction (H_c) combining equations (1) and (12):

$$H_c = \frac{H_{O-P}}{C + 1} \quad (15)$$

where H_{O-P} was extracted from the nanoindentation test data using the standard Oliver-Pharr method.

However, only between 11-30 topography maps of indentation prints were made for each investigated grade, corresponding to 15 - 35 % of indents at each grade. Two different contact area correction approaches were used. The first approach is based on the assumption that indents with similar angles should have a similar contact area correction coefficient. Equation (13) was used to estimate C , which was then used to determination the corrected hardness values (H_c) using (15). This method is less accurate than the approach detailed below; however, it allows hardness data correction without requiring time-consuming experimental profilometry mapping of every indent.

The second approach was based on the elastic-modulus-based correction method which has been successfully applied in ferritic-martensitic steel (Heintze et al., 2016) and tungsten alloys (Beck et al., 2017). The method is based on the assumption, that as the contact area affects both hardness and indentation elastic modulus calculations (see equations (1) and (3)), then, in a material with known indentation modulus and Poisson's ratio, it should be possible to calculate the area correction coefficient from the measured modulus without having to image the indents at all. This data correction method can also be used for data from indents on or near to grain-boundaries, where no unambiguous crystallographic information is available. In this method, the area correction coefficient was deduced by combining equations (2), (3) and (12):

$$C_E = \left(\frac{\frac{1 - \nu^2}{\langle E \rangle} + \frac{1 - \nu_i^2}{E_i}}{\frac{1 - \nu^2}{E_{O-P}} + \frac{1 - \nu_i^2}{E_i}} \right)^2 - 1 \quad (16)$$

where E_{O-P} is the indentation modulus obtained according to Oliver and Pharr (Oliver and Pharr, 1992) without pile-up/sink-in considerations and $\langle E \rangle$ is the measured indentation elastic modulus of the material. As demonstrated in the previous section, the measured indentation elastic modulus of 296 GPa is in good agreement with the Young's modulus of industrial polycrystalline beryllium. This value was used for $\langle E \rangle$ in equation (16). The corrected hardness obtained with this method is denoted:

$$H_E = \frac{H_{O-P}}{(C_E + 1)} \quad (17)$$

Both C and C_E were used for correcting the nanoindentation hardness data where the crystallographic orientation of the indented areas were confidently known (i.e. inside grains), and C_E was used for data analysis of indents made close to grain boundaries. Figure 10 **Error! Reference source not found.** compares hardness data from four beryllium grades before and after the corrections and shows that while H_E exhibits higher scatter and suggest slightly smaller anisotropy relative to H_C , both correction approaches showed reasonable agreement. The numeric values describing the observed trends are summarised in Table 1.

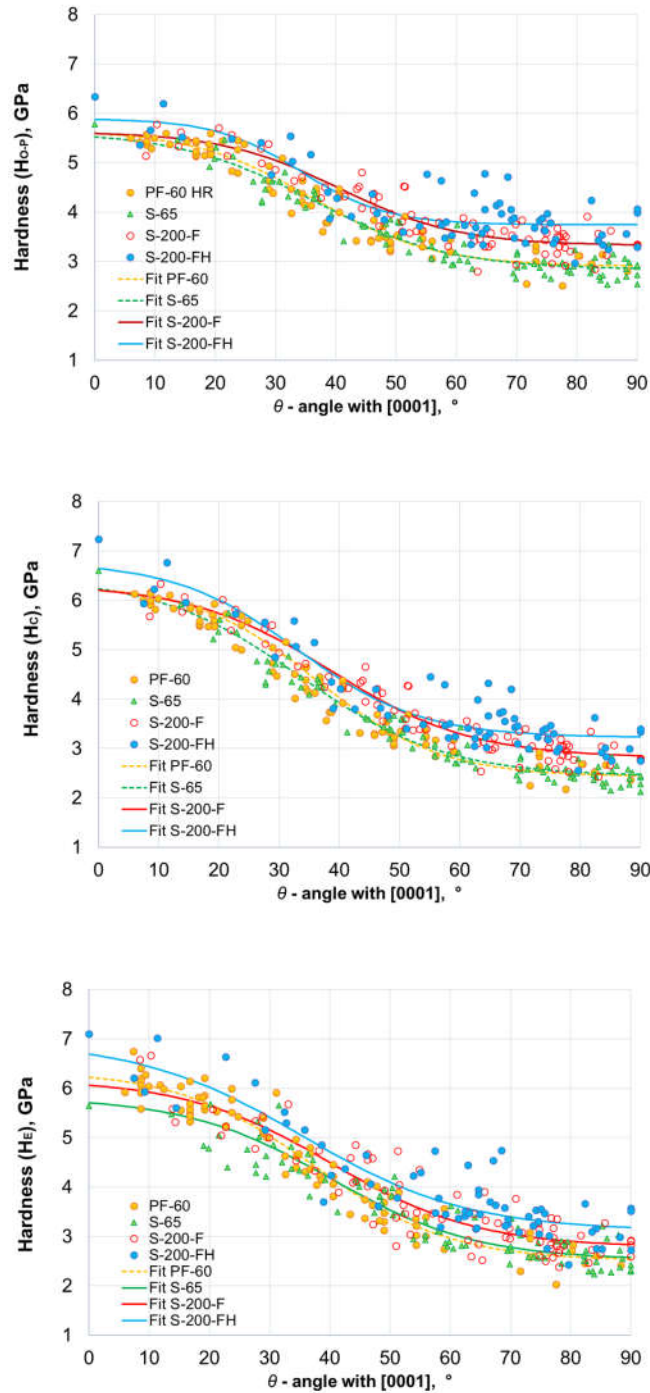


Figure 10. Nanoindentation hardness from 4 beryllium grades for different crystallographic orientation, calculated with the: (a) Oliver-Pharr method (Oliver and Pharr, 1992), (b) corrected via profilometry data using equations (13) and (15), (c) corrected via comparison of measured and known modulus using equation (17). 0° corresponds to indentation into the basal plane parallel to the [0001] direction, 90° implies indentation perpendicular to [0001]. Only data from grains with the assigned crystallographic orientation are shown (no data from indents on or close to grain boundaries). Hardness with indentation parallel to [0001] is double that for orientations perpendicular to [0001]. Lines show fitting of the experimental data to Boltzmann type sigmoidal curves.

Figure 10 shows that the nanoindentation hardness as a function of indentation angle has a characteristic sigmoid shape with maximum and minimum hardness for indentation directions (test surface plane normals) parallel and perpendicular to [0001] respectively. Similar trends were observed in the micro- and macro-hardness tests performed in beryllium monocrystals by (Tsuya, 1967) and (Hill and Jones, 1961).

For ease of comparison, the experimentally observed relation between the indentation angle (θ) and the hardness data was fitted to a Boltzmann type sigmoidal curve:

$$H(\theta) = \frac{H_{max} - H_{min}}{1 + \exp\left(\frac{\theta - \theta_0}{S}\right)} + H_{min} \quad (18)$$

where hardness varies from H_{max} to H_{min} , θ_0 is the angle at which the hardness is halfway between H_{max} and H_{min} , and S describes the steepness of the curve. The fitting parameters together with the R^2 coefficient are shown in Table 1. Since a large number of indents had θ close to 90° , the fitting parameter H_{min} is a good approximation of the average hardness for the soft orientation. Unfortunately, only limited data were available for indentation close to [0001] and given the observed scatter, the fitted H_{max} parameter may not accurately represent the “hard” grain hardness.

Figure 10 and Table 1 demonstrate that high purity grades PF-60 and S-65 had almost identical hardness for the same crystallographic orientation, whereas S-200-F and particularly S-200-HF had noticeably higher hardness, especially for soft orientations. The difference may originate from impurity effects. It is likely that the S-200-F has a higher content of oxygen, carbon, iron, aluminium silicon and magnesium (see Table 1). Aldinger (D. Webster, 2012) demonstrated that the critical resolved shear stresses (CRSS) for both basal and prismatic slip in beryllium is proportional to $c^{2/3}$, where c is the impurity concentration in wt%, for a wide range of impurity types. The increased CRSS values could explain higher hardness for the less pure grade, but detailed fine-scale chemical analysis of the S-200 grade is needed for confirmation.

	PF-60			S-65			S-200-F			S-200-FH		
	H _{O-P} ²⁾	H _C ³⁾	H _E ⁴⁾	H _{O-P}	H _C	H _E	H _{O-P}	H _C	H _E	H _{O-P}	H _C	H _E
H _{min} (\perp to [0001]) ¹⁾ , GPa	2.9	2.4	2.5	2.8	2.4	2.5	3.3	2.8	2.7	3.7	3.2	3.2
H _{max} (\parallel to [0001]) ¹⁾ , GPa	5.7	6.3	6.4	5.6	6.5	5.9	5.6	6.3	5.9	5.9	6.8	6.7
mid point angle (θ_0) ¹⁾ , deg	36.2	36.3	37.3	36.2	33.6	40.2	40.7	38.7	42.0	34.3	33.1	36.8
Slope (S) ¹⁾	10.0	10.2	11.3	11.3	12.0	12.1	9.9	11.7	10.1	7.1	10.2	11.4
R ² ¹⁾	0.89	0.94	0.90	0.91	0.94	0.81	0.86	0.93	0.81	0.74	0.87	0.82
Average hardness, GPa	4.5±0.8	-	4.7±0.9	3.7±0.6	-	3.5±0.8	4.1±0.5	-	3.9±0.8	4.5±0.7	-	4.5±0.8
Average hardness inside grains, GPa	4.3±0.8	4.4±1.1	4.6±1.1	3.5±0.7	3.3±0.8	3.4±0.8	3.9±0.6	3.7±0.8	3.7±0.8	4.0±0.6	3.9±0.8	4.1±1.0
Indentation modulus, GPa	291±14	291±9	296 ⁵⁾	303±14	291±11	296	312±18	299±13	296	306±17	294±10	296
Hardness at or near grain boundaries, GPa	4.8±0.6	-	5.0±0.6	3.8±0.6	-	3.8±0.8	4.2±0.5	-	4.0±0.6	4.7±0.7	-	4.7±0.8
Grain size, μm	25 ± 14			7.3± 4.4			7.1 ± 4.1			5.3 ± 3.3		
Minimum Be content ⁶⁾ , %	99.2			99.0			98.5			98.5		
Main impurities content ⁶⁾ , appm	O=2900, C=450, Fe=130 Al=165, Si=130, N=195			O=3260, C=680, Fe=130 Al=170, Si=145			O=5450, C=1150, Fe=210 Al=340, Si=193, Mg=130			O=5450, C=1150, Fe=210 Al=340, Si=193, Mg=130		

¹⁾ Boltzmann type sigmoidal curve fitting parameters (equation (18)) for nanoindentation harnesses of different beryllium grades as functions of indentation angle with the [0001] crystallographic direction

²⁾ Calculated using the standard Oliver-Pharr algorithm (Oliver and Pharr, 1992).

³⁾ Contact area corrected data using equation (15) which considers pile-up/sink-in contribution using the crystallographically dependent area correction coefficient calculated with equation (13).

⁴⁾ Contact area corrected data using equation (17) which considers pile-up/sink-in contribution based on the expected indentation modulus-based approach

⁵⁾ fixed value of 296 GPa is used for the data correction

⁶⁾ The nominal chemical compositions of the grades, which specify maximum content of different impurities, (Materion Electrofusion Corporation)

Table 1. Nanoindentation, microstructural and chemical composition data from four beryllium grades

The change in average hardness due to the pile-up / sink-in corrections was less than 5%, see Table 1. When corrected, the hardness H_{max} increased in hard orientations (due to sink-ins) whereas the hardness in soft orientations H_{min} was reduced. Therefore hardness values derived from the O-P method underestimate the hardness anisotropy.

Table 1 also compares the average corrected H_E and non-corrected H_{O-P} hardness obtained from grains and grain boundaries. In both cases, the hardness from indents in grain centres was 10% lower than from those at grain boundaries. This may result from extra stress needed to transfer dislocations across grain boundaries or from impurity precipitates which are mainly located at grain boundaries in VHP and HIP-ed grades (see Figure 2(b), (c), and (d)). The hot rolled PF-60 grade grain boundaries are free of visible precipitates (Figure 2(a)), but it is known that in this grade, grain boundaries have noticeable iron segregation (Kuksenko et al., 2017) which could possibly contribute to GB hardening.

3.2.6 Hardness anisotropy

Figure 11 shows the orientation dependence of experimentally-determined hardness values, as a function of position of the indentation direction within the unit stereographic triangle. No distinct variation in hardness with angle between the $[10\bar{1}0]$ and $[11\bar{2}0]$ directions was found; this is in good agreement with our CPFEM results. This also agrees with the results of Tsuya (Tsuya, 1967) on single crystals Vickers indentation, who also demonstrated no significant difference in hardness of the $(10\bar{1}0)$ and $(11\bar{2}0)$ planes.

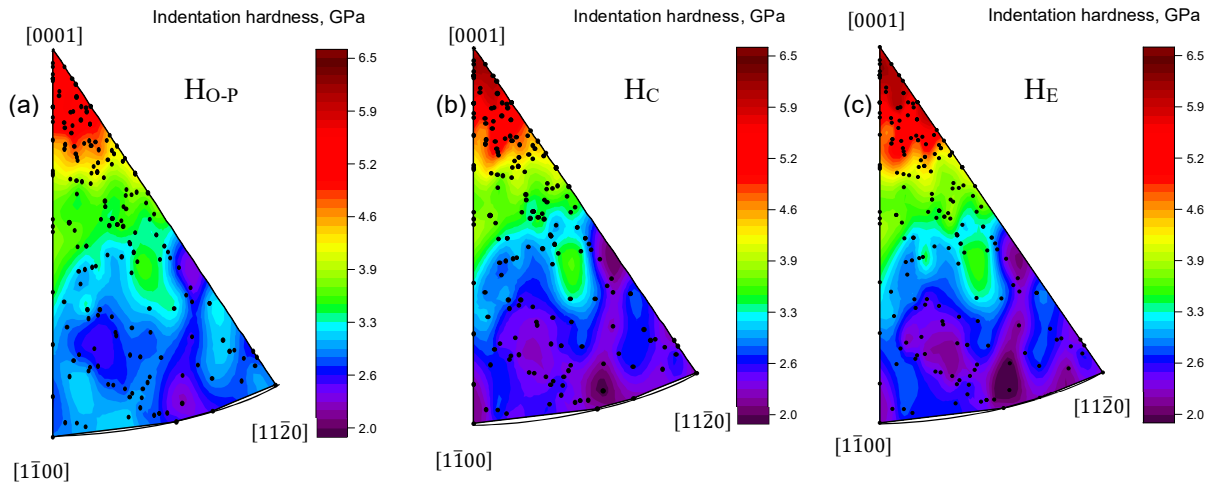


Figure 11. Pole figure of the nanoindentation hardness: (a) H_{O-P} , calculated with the Oliver-Pharr method; (b) H_C hardness corrected assuming the correction coefficient C given in equation (13) (c) H_E elastic-modulus-corrected values. The data set consist of 217 indents in the high-purity PF-60 and S65 grades. Experimental measurement data points are shown as black dots.

The H_{max}/H_{min} ratio obtained using the Oliver-Pharr approach is about 1.98 in the high-purity grades and 1.65 in the low purity grades, and after the area correction, they increase to 2.62 and 2.21 respectively. This is higher than in other common hcp metals. An H_{max}/H_{min} ratio between 1.25 and 1.5 was measured in titanium (Britton et al., 2010; Zambaldi et al., 2012) and α phase of a Ti-6Al-4V alloy (Viswanathan et al., 2005). $H_{max}/H_{min}=1.14$ was observed in single-crystalline zinc (Vlassak and

Nix, 1994). An H_{max}/H_{min} ratio value of about 1.17 was measured in single-crystalline magnesium (Somekawa and Schuh, 2016), but in this case the prismatic plane hardness was harder than the basal plane.

To our knowledge, this is the first nanoindentation study which compares different crystallographic orientation in beryllium, however some macro- and microhardness data obtained with 4-sided Vickers pyramid tip is available. The nanoindentation Berkovich tip was designed to have the same ratio of projected area to indentation depth as the Vickers indenter and both indenters have the same representative strain within the specimen material (Fischer-Cripps, 2004), therefore, the similar H_{max}/H_{min} ratios are expected from the two tip geometries (Rother et al., 1998). H_{max}/H_{min} ratios of 2.24 and 2.55 using Vickers indentation with 200g and 2kg loads respectively were obtained by Hill and Jones (Hill and Jones, 1961) from indentation of a single crystal beryllium of unspecified purity. A ratio of 2.78 was observed by Tsuya (Tsuya, 1967) from Vickers hardness measurements of the hard (0001) plane and soft (10 $\bar{1}$ 0) and (11 $\bar{2}$ 0) planes in the low-purity single crystal beryllium (300g load). Both previous experiments with Vickers tips (Hill and Jones, 1961; Tsuya, 1967) are in good agreement with our H_{max}/H_{min} ratio obtained from nanoindentation data, but only if the pile-up/sink-in contact area correction is performed. Considering this, it is important to emphasize that while the average nanoindentation hardness of the beryllium samples investigated here remained almost unchanged after the contact area correction, such corrections are important for description and comparison of nanoindentation hardness data between different grades or sample treatments.

4 Conclusion

High variation in nanoindentation hardness was observed in four industrial beryllium grades. It was demonstrated that the crystallographic orientation of the indented grains is the major source of the wide scattering of hardness values and the hardness measured by indentation into grain with surface normal close to the [0001] c-axis of beryllium is $\sim 2.6x$ higher than for indentations into grains with surface normal directions close to [11 $\bar{2}$ 0] or [1 $\bar{1}$ 00] in high-purity beryllium grades, and 2.2 higher in

low-purity grades. This is related to the anisotropy of plastic deformation in grains with different orientations, as demonstrated by CPFEM simulations. The difference between low-purity and high-purity grades was mainly in hardness data when indenting into soft grains.

Experiments and simulations demonstrated that localised surface deformation around indentation prints (pile-up and sink-in) is highly crystallographically dependent: the sink-in behaviour dominated in hard grains (those indented close to the c-axis) while in soft grains (indented orthogonal to the c axis) pile-ups dominated. Topography investigations of the residual indentation prints demonstrated that when compared to the contact area calculated by the standard Oliver-Pharr method, the actual contact area is reduced by 10 to 20% in hard grains, whereas in soft grains the actual contact area is increased by approximately 25%. Evaluation of the hardness data and comparison with earlier studies demonstrated that the contact area correction is a key procedure for description of nanoindentation hardness between different grades or sample treatments of beryllium.

Two different contact area correction methods were applied and showed good agreement between each other and the data corrected by actual topography investigation of residual indentation prints.

No unambiguous link between the indentation modulus and the crystallography of the grain was observed. This is due to the fact that elastic interaction between the indenter and the sample for the chosen indentation depth, as demonstrated by CPFEM analysis, is much larger than the materials' grain size.

5 Acknowledgments

This work was supported by the Fermi Research Alliance, LLC under Contract No. DE-AC02-07CH11359 with the United States Department of Energy, and by the UK Science and Technology Facilities Council. We thank Patrick Hurh (Fermi National Accelerator Laboratory, USA) and Chris Densham (Rutherford Appleton Laboratory, Didcot, UK) who supported this work and the RaDIATE project within which the experiments were performed. E. Tarleton acknowledges the Engineering and Physical Sciences Research Council, fellowship grant EP/N007239/1. We thank Prof. F. Dunne for providing a copy of his UEL code.

6 References

- ‘Abaqus 2016 Documentation’, 2016. , Dassault Systèmes, Providence, RI, USA.
- Arsenlis, A., Parks, D., 1999. Crystallographic aspects of geometrically-necessary and statistically-stored dislocation density. *Acta Mater.* 47, 1597–1611. [https://doi.org/10.1016/S1359-6454\(99\)00020-8](https://doi.org/10.1016/S1359-6454(99)00020-8)
- Beck, C.E., Hofmann, F., Eliason, J.K., Maznev, A.A., Nelson, K.A., Armstrong, D.E.J., 2017. Correcting for contact area changes in nanoindentation using surface acoustic waves. *Scr. Mater.* 128, 83–86. <https://doi.org/10.1016/j.scriptamat.2016.09.037>
- Bolshakov, A., Pharr, G.M., 1998. Influences of pileup on the measurement of mechanical properties by load and depth sensing indentation techniques. *J. Mater. Res.* 13, 1049–1058. <https://doi.org/10.1557/JMR.1998.0146>
- Britton, T.B., Liang, H., Dunne, F.P.E., Wilkinson, A.J., 2010. The effect of crystal orientation on the indentation response of commercially pure titanium: experiments and simulations. *Proc. R. Soc. Lond. Math. Phys. Eng. Sci.* 466, 695–719. <https://doi.org/10.1098/rspa.2009.0455>
- Brookes, C.A., O’Neill, J.B., Redfern, B. a. W., 1971. Anisotropy in the hardness of single crystals. *Proc R Soc Lond A* 322, 73–88. <https://doi.org/10.1098/rspa.1971.0055>
- Brown, D.W., Beyerlein, I.J., Sisneros, T.A., Clausen, B., Tomé, C.N., 2012. Role of twinning and slip during compressive deformation of beryllium as a function of strain rate. *Int. J. Plast.* 29, 120–135. <https://doi.org/10.1016/j.ijplas.2011.08.006>
- Bunshah, R.F., Armstrong, R.W., 1969. The dependence of the hardness of beryllium on grain size. *Mater. Res. Bull.* 4, 239–249. [https://doi.org/10.1016/0025-5408\(69\)90099-3](https://doi.org/10.1016/0025-5408(69)90099-3)
- Chakin, V.P., Posevin, A.O., Kupriyanov, I.B., 2007. Swelling, mechanical properties and microstructure of beryllium irradiated at 200°C up to extremely high neutron doses. *J. Nucl. Mater.* 367–370, 1377–1381. <https://doi.org/10.1016/j.jnucmat.2007.03.253>
- Christman, D.R., Feistmann, F.J., 1972. Dynamic Properties of S-200-E Beryllium. PN, MANUFACTURING DEVELOPMENT 6 GENERAL MOTORS CORPORATION.
- D. Webster, 2012. *Beryllium Science and Technology*. Springer Verlag.
- Delafargue, A., Ulm, F.-J., 2004. Explicit approximations of the indentation modulus of elastically orthotropic solids for conical indenters. *Int. J. Solids Struct.* 41, 7351–7360. <https://doi.org/10.1016/j.ijsolstr.2004.06.019>
- Design Guides for Materion Beryllium Metal, 2017. . Materion.
- Dunne, F.P.E., Kiwanuka, R., Wilkinson, A.J., 2012. Crystal plasticity analysis of micro-deformation, lattice rotation and geometrically necessary dislocation density. *Proc. R. Soc. Math. Phys. Eng. Sci.* 468, 2509–2531. <https://doi.org/10.1098/rspa.2012.0050>
- Dunne, F.P.E., Rugg, D., Walker, A., 2007. Lengthscale-dependent, elastically anisotropic, physically-based hcp crystal plasticity: Application to cold-dwell fatigue in Ti alloys. *Int. J. Plast.* 23, 1061–1083. <https://doi.org/10.1016/j.ijplas.2006.10.013>
- Fischer-Cripps, A.C., 2004. *Nanoindentation*, Mechanical Engineering Series. Springer New York, New York, NY. <https://doi.org/10.1007/978-1-4757-5943-3>
- Gwyddion – Applications - <http://gwyddion.net/> [WWW Document], 2018. URL <http://gwyddion.net/> (accessed 10.23.17).
- Hardie, C.D., Roberts, S.G., Bushby, A.J., 2015. Understanding the effects of ion irradiation using nanoindentation techniques. *J. Nucl. Mater.* 462, 391–401. <https://doi.org/10.1016/j.jnucmat.2014.11.066>
- Haušild, P., Materna, A., Nohava, J., 2014. Characterization of Anisotropy in Hardness and Indentation Modulus by Nanoindentation. *Metallogr. Microstruct. Anal.* 3, 5–10. <https://doi.org/10.1007/s13632-013-0110-8>

- Heintze, C., Bergner, F., Akhmadaliev, S., Altstadt, E., 2016. Ion irradiation combined with nanoindentation as a screening test procedure for irradiation hardening. *J. Nucl. Mater.* 472, 196–205. <https://doi.org/10.1016/j.jnucmat.2015.07.023>
- Hill, N.A., Jones, J.W.S., 1961. The crystallographic dependence of low load indentation hardness in beryllium. *J. Nucl. Mater.* 3, 138–155. [https://doi.org/10.1016/0022-3115\(61\)90002-2](https://doi.org/10.1016/0022-3115(61)90002-2)
- Hirsch, P.B., Pirouz, P., Roberts, S.G., Warren, P.D., 1985. Indentation plasticity and polarity of hardness on 111 faces of GaAs. *Philos. Mag. B* 52, 759–784. <https://doi.org/10.1080/13642818508240635>
- ISO 14577-1, 2015. , in: *Metallic Materials -- Instrumented Indentation Test for Hardness and Materials Parameters -- Part 1: Test Method.*
- Kese, K.O., Li, Z.C., Bergman, B., 2005. Method to account for true contact area in soda-lime glass during nanoindentation with the Berkovich tip. *Mater. Sci. Eng. A* 404, 1–8. <https://doi.org/10.1016/j.msea.2005.06.006>
- Knezevic, M., Beyerlein, I.J., Brown, D.W., Sisneros, T.A., Tomé, C.N., 2013. A polycrystal plasticity model for predicting mechanical response and texture evolution during strain-path changes: Application to beryllium. *Int. J. Plast.* 49, 185–198. <https://doi.org/10.1016/j.ijplas.2013.03.008>
- Kuksenko, V., Ammigan, K., Hartsell, B., Densham, C., Hurh, P., Roberts, S., 2017. Irradiation effects in beryllium exposed to high energy protons of the NuMI neutrino source. *J. Nucl. Mater.* 490, 260–271. <https://doi.org/10.1016/j.jnucmat.2017.04.011>
- McElhaney, K.W., Vlassak, J.J., Nix, W.D., 1998. Determination of indenter tip geometry and indentation contact area for depth-sensing indentation experiments. *J. Mater. Res.* 13, 1300–1306. <https://doi.org/10.1557/JMR.1998.0185>
- OIM Analysis™/ EDAX [WWW Document], 2018. URL <https://www.edax.com/products/ebsd/oim-analysis> (accessed 4.9.18).
- Oliver, W.C., Pharr, G.M., 1992. An improved technique for determining hardness and elastic modulus using load and displacement sensing indentation experiments. *J. Mater. Res.* 7, 1564–1583. <https://doi.org/10.1557/JMR.1992.1564>
- PF-60 Beryllium Foil for X-ray [WWW Document], 2018. URL <http://materion.com/Products/Beryllium/BerylliumX-Ray/X-ray-PF-60.aspx> (accessed 3.26.18).
- Renner, E., Gaillard, Y., Richard, F., Amiot, F., Delobelle, P., 2016. Sensitivity of the residual topography to single crystal plasticity parameters in Berkovich nanoindentation on FCC nickel. *Int. J. Plast.* 77, 118–140. <https://doi.org/10.1016/j.ijplas.2015.10.002>
- Rother, B., Steiner, A., Dietrich, D.A., Jehn, H.A., Haupt, J., Gissler, W., 1998. Depth-sensing indentation measurements with Vickers and Berkovich indenters. *J. Mater. Res.* 13, 2071–2076. <https://doi.org/10.1557/JMR.1998.0291>
- S-65 Nuclear Grade Beryllium - Materion [WWW Document], 2018. URL <https://materion.com/Products/Beryllium/Beryllium-Metal/S-65.aspx> (accessed 3.26.18).
- S-200-F - Materion [WWW Document], 2018. URL <https://materion.com/Products/Beryllium/Beryllium-Metal/S-200F.aspx> (accessed 3.26.18).
- S-200-F H - Materion [WWW Document], 2018. URL <https://materion.com/Products/Beryllium/Beryllium-Metal/S-200-FH.aspx> (accessed 3.26.18).
- Somekawa, H., Schuh, C.A., 2016. Effect of Crystal Orientation on Nanoindentation Behavior in Magnesium. *Metall. Mater. Trans. A* 47, 3227–3234. <https://doi.org/10.1007/s11661-016-3479-6>
- Su, Y., Zambaldi, C., Mercier, D., Eisenlohr, P., Bieler, T.R., Crimp, M.A., 2016. Quantifying deformation processes near grain boundaries in α titanium using nanoindentation and crystal plasticity modeling. *Int. J. Plast.* 86, 170–186. <https://doi.org/10.1016/j.ijplas.2016.08.007>

- Tsuya, K., 1967. The effect of temperature on the hardness anisotropy of beryllium single crystals. *J. Nucl. Mater.* 22, 148–157. [https://doi.org/10.1016/0022-3115\(67\)90024-4](https://doi.org/10.1016/0022-3115(67)90024-4)
- Viswanathan, G.B., Lee, E., Maher, D.M., Banerjee, S., Fraser, H.L., 2005. Direct observations and analyses of dislocation substructures in the α phase of an α/β Ti-alloy formed by nanoindentation. *Acta Mater.* 53, 5101–5115. <https://doi.org/10.1016/j.actamat.2005.07.030>
- Vlassak, J.J., Nix, W.D., 1994. Measuring the elastic properties of anisotropic materials by means of indentation experiments. *J. Mech. Phys. Solids* 42, 1223–1245. [https://doi.org/10.1016/0022-5096\(94\)90033-7](https://doi.org/10.1016/0022-5096(94)90033-7)
- Walsh, K.A., 2009. *Beryllium Chemistry and Processing*. ASM International.
- Wardle, S.T., Lin, L.S., Cetel, A., Adams, B.L., 1994. Orientation imaging microscopy: Monitoring residual stress profiles in single crystals using an image-quality parameter, IQ, in: *Proceedings of the Annual Meeting-Electron Microscopy Society of America*. SAN FRANCISCO PRESS, pp. 680–680.
- Zambaldi, C., Yang, Y., Bieler, T.R., Raabe, D., 2012. Orientation informed nanoindentation of α -titanium: Indentation pileup in hexagonal metals deforming by prismatic slip. *J. Mater. Res.* 27, 356–367. <https://doi.org/10.1557/jmr.2011.334>